GPS Solutions (2026) 30:23
https://doi.org/10.1007/s10291-025-01991-w

RESEARCH

Inequality-constrained integer least-squares and its application to troposphere-bounded GNSS PPP

Andreas Brack[1] · **Shengping He**[1]

Received: 23 July 2025 / Accepted: 29 October 2025

Abstract
In GNSS precise point positioning (PPP), a user commonly estimates a troposphere parameter representing the zenith wet delay (ZWD). The ZWD is non-negative and generally assumes values of up to around 30 cm. In the initial epochs of a PPP solution, however, the precision of the estimated ZWD parameter can be on the several meter level, most likely leading to unrealistic ZWD estimates outside of this interval, and large errors in the up component. In this contribution, we introduce and discuss a troposphere-bounded GNSS model, in which the ZWD parameter is constrained to an a-priori defined feasible interval. This translates to an observation model with linear inequality constraints, for which we derive and discuss two solutions, the constrained float solution and the constrained integer least-squares (ILS) solution. We analyze the positioning capabilities of the troposphere-bounded model as compared to the unconstrained case by means of simulated multi-frequency GPS and Galileo PPP examples and exemplary real-data experiments. With the constrained ambiguity-float solution, the RMS error of the up component is improved by up to 75% for GPS and up to 65% for GPS+Galileo solutions in the first observation epochs, even for relatively loose ZWD constraint intervals of 20 cm or more. The constrained ILS solution leads to higher ambiguity success rates, so that for instance ZWD constraint intervals of five and 20 cm reduce the average times-to-first-fix the ambiguities by around 17.5% and 10%.

Keywords Multi-GNSS · Troposphere · Zenith wet delay · Constrained integer least-squares · Ambiguity resolution · PPP · PPP-RTK

Introduction

In high-precision global navigation satellite system (GNSS) applications such as precise point positioning (PPP), with ambiguity-resolution also referred to as PPP-RTK, it is required to account for atmospheric effects. GNSS signals are delayed while crossing the troposphere, where it is usually distinguished between the hydrostatic and the wet delay component. Both components can be represented by the delay in zenith direction from the receiver and satellite-specific mapping factors accounting for the direction of the satellite, using for instance the global mapping function (GMF, Böhm et al. 2006) or the Vienna mapping functions (VMF, Böhm and Schuh 2004). The hydrostatic delay accounts for ~ 90% of the total tropospheric delay. It only depends on the pressure and geolocation and can be precisely modeled, e.g. with the semi-empirical Saastamoinen model (Saastamoinen 1972) with observed or modeled ground pressure (e.g. from GPT2, Lagler et al. 2013). The wet tropospheric delay is difficult to be precisely modeled, as it is affected by the high spatial and temporal variations of water vapor. In the following, we briefly outline different ways how the wet tropospheric delay can be handled, together with the corresponding observation models.

The weakest model is the *troposphere-float model* (Kleijer 2004), in which a parameter for the zenith wet delay (ZWD) of the receiver is set up and estimated along with the other parameters. This strategy is commonly used in most high-precision positioning applications (Zumberge et al. 1997). Due to the observation geometry, the ZWD estimate is highly correlated with the estimated up component of the user position (Vaclavovic et al. 2017).

The strongest model is the *troposphere-fixed model* (Kleijer 2004), in which the tropospheric delay is assumed

✉ Andreas Brack
brack@gfz.de

[1] GFZ Helmholtz Centre for Geosciences, Telegrafenberg, 14473 Potsdam, Germany

Published online: 12 November 2025

to be completely corrected for and no ZWD parameter is estimated. This model can typically be applied for short baseline positioning or in PPP when using corrections from a local reference network (Teunissen et al. 2010), when the differences of the tropospheric delays between the receivers are negligible. Removing the ZWD parameter from the observation model mostly improves the precision of the estimated up component in positioning applications, in particular for short observation time spans.

A trade-off between the troposphere-float and -fixed models is the *troposphere-weighted model* (Kleijer 2004), in which a-priori information about the ZWD is included as pseudo observation and weighted according to its uncertainty. If the uncertainty is assumed very large, the troposphere-weighted model converges to the troposphere-float model, whereas for vanishing uncertainty the troposphere-weighted model becomes identical to the troposphere-fixed model. This model can for instance be applied by PPP users when utilizing numerical weather prediction models to calculate the approximate ZWD (Wilgan et al. 2017) or when interpolating network derived ZWD parameters (de Oliveira Jr et al. 2017; Gao et al. 2024). The troposphere-weighted model can also be used to constrain the time-differenced ZWD to account for its relatively slow variability, for instance in the form of a random-walk process (Hadas et al. 2017).

In this contribution, we introduce a GNSS observation model in which the ZWD parameter is *bounded through inequality constraints*, an idea that was introduced in He (2025). The bounds can for instance be derived from the physical properties of the troposphere, utilizing feasible limits of the ground temperature and the relative humidity in ZWD models. As an example, a simple but already useful lower bound corresponding to zero relative humidity is that the ZWD is non-negative. This model can prove particularly useful in real-time applications, as it does not rely on the availability of external ZWD information. By constraining the ZWD parameter we want to improve the positioning performance, while the dependence on external tropospheric corrections and their associated uncertainties is avoided.

In contrast to the above mentioned tropospheric models, this troposphere-bounded model can no longer be solved by the standard least-squares and integer least-squares (ILS) methods. The constraints should be fully integrated into the objective function, resulting in an *(integer) least-squares problem with linear inequality constraints*. Rigorously including constraints on the real-valued parameters in an ILS problem has previously been formulated in the GNSS compass model (Park and Teunissen 2009; Teunissen 2010; Teunissen et al. 2011) and in the GNSS attitude model (Teunissen 2007; Giorgi et al. 2012), both making use of non-linear equality constraints on the local geometry of a multi-receiver setup. Khodabandeh (2022) formulated a bias-bounded model, which allows one to resolve integer ambiguities in rank-deficient models. Our ILS problem with linear inequality constraints can be solved in a similar way as the GNSS compass and attitude models, making use of the same orthogonal decomposition of the objective function.

The expected benefits of the troposphere-bounded solution compared to the unconstrained model are twofold: Firstly, the accuracy of the ambiguity-float solution should be improved, in particular for the up component, and secondly, the ILS success rate (SR) should be increased, leading to shorter convergence times.

This contribution is organized as follows. We first introduce the GNSS observation model with arbitrary constraints on the real-valued parameters and recap its constrained (integer) least-squares solution that follows from rigorously including the constraint into the ambiguity objective function. We then formulate, as one specific example, the troposphere-bounded model and derive its solution together with a discussion of the distributional properties. The performance of the troposphere-bounded model is finally analyzed in PPP/PPP-RTK examples using simulated and real GNSS data.

The GNSS observation model and its constrained least-squares solution

Let the linear(ized) full-rank model of the GNSS observation vector $\boldsymbol{y} \in \mathbb{R}^m$ containing the observed minus computed phase and/or code measurements be given by

$$\boldsymbol{y} = \boldsymbol{A}\boldsymbol{a} + \boldsymbol{B}\boldsymbol{b} + \boldsymbol{\eta}, \tag{1}$$

with $\boldsymbol{a} \in \mathbb{Z}^n$ the vector of integer ambiguity parameters, $\boldsymbol{b} \in \mathcal{B} \subseteq \mathbb{R}^p$ the vector of real-valued parameters such as incremental receiver coordinates, the ZWD, clock offsets, or instrumental and ionospheric delays, and $\boldsymbol{A}$ and $\boldsymbol{B}$ the known design matrices. The additive noise vector $\boldsymbol{\eta} \in \mathbb{R}^m$ is assumed as zero-mean Gaussian with covariance matrix $\boldsymbol{Q_y}$.

Applying the least-squares principle to (1) results in the following minimization problem

$$\min_{\boldsymbol{z}\in\mathbb{Z}^n, \boldsymbol{\beta}\in\mathcal{B}} \|\boldsymbol{y} - \boldsymbol{A}\boldsymbol{z} - \boldsymbol{B}\boldsymbol{\beta}\|^2_{\boldsymbol{Q_y}}. \tag{2}$$

When no constraints are imposed on $\boldsymbol{b}$ so that $\mathcal{B} = \mathbb{R}^p$, which is usually the case in conventional PPP models, (2) is called an *integer least-squares* (ILS) problem (Teunissen

1993). Depending on the application at hand, additional information on the properties of $\boldsymbol{b}$ might be available that can be included by restricting the feasible set $\mathcal{B}$ of $\boldsymbol{b}$ when solving (1) for the unknown parameter vectors $\boldsymbol{a}$ and $\boldsymbol{b}$.

The solution of (2) can be derived by making use of the orthogonal decomposition (Teunissen 1993)

$$\begin{aligned}\|\boldsymbol{y}-\boldsymbol{A}\boldsymbol{z}-\boldsymbol{B}\boldsymbol{\beta}\|^2_{\boldsymbol{Q}_y} &= \|\hat{\boldsymbol{e}}\|^2_{\boldsymbol{Q}_y}+\|\hat{\boldsymbol{a}}-\boldsymbol{z}\|^2_{\boldsymbol{Q}_{\hat{a}}}\\ &\quad+\|\hat{\boldsymbol{b}}(\boldsymbol{z})-\boldsymbol{\beta}\|^2_{\boldsymbol{Q}_{\hat{b}(\boldsymbol{z})}},\end{aligned} \tag{3}$$

where $\hat{\boldsymbol{e}}=\boldsymbol{y}-\boldsymbol{A}\hat{\boldsymbol{a}}-\boldsymbol{B}\hat{\boldsymbol{b}}$ is the least-squares residual vector with the unconstrained float solutions $\hat{\boldsymbol{a}}$ and $\hat{\boldsymbol{b}}$ from a linear least-squares adjustment, whose variance and covariance matrices are denoted by $\boldsymbol{Q}_{\hat{a}}$, $\boldsymbol{Q}_{\hat{b}}$, and $\boldsymbol{Q}_{\hat{a}\hat{b}}$. The conditional float solution $\hat{\boldsymbol{b}}(\boldsymbol{z})=\hat{\boldsymbol{b}}-\boldsymbol{Q}_{\hat{b}\hat{a}}\boldsymbol{Q}^{-1}_{\hat{a}}(\hat{\boldsymbol{a}}-\boldsymbol{z})$, with variance matrix $\boldsymbol{Q}_{\hat{b}(\boldsymbol{z})}=\boldsymbol{Q}_{\hat{b}}-\boldsymbol{Q}_{\hat{b}\hat{a}}\boldsymbol{Q}^{-1}_{\hat{a}}\boldsymbol{Q}_{\hat{a}\hat{b}}$ assumes that the value of the unknown ambiguity vector $\boldsymbol{a}$ is given by $\boldsymbol{z}$. The minimization problem (2) can now be written as

$$\begin{aligned}&\min_{\boldsymbol{z}\in\mathbb{Z}^n,\boldsymbol{\beta}\in\mathcal{B}}\|\boldsymbol{y}-\boldsymbol{A}\boldsymbol{z}-\boldsymbol{B}\boldsymbol{\beta}\|^2_{\boldsymbol{Q}_y}=\|\hat{\boldsymbol{e}}\|^2_{\boldsymbol{Q}_y}\\ &+\min_{\boldsymbol{z}\in\mathbb{Z}^n}\left(\|\hat{\boldsymbol{a}}-\boldsymbol{z}\|^2_{\boldsymbol{Q}_{\hat{a}}}+\min_{\boldsymbol{\beta}\in\mathcal{B}}\|\hat{\boldsymbol{b}}(\boldsymbol{z})-\boldsymbol{\beta}\|^2_{\boldsymbol{Q}_{\hat{b}(\boldsymbol{z})}}\right).\end{aligned} \tag{4}$$

Let the minimizer of the third term be denoted as

$$\check{\boldsymbol{b}}(\boldsymbol{z})=\underset{\boldsymbol{\beta}\in\mathcal{B}}{\operatorname{argmin}}\|\hat{\boldsymbol{b}}(\boldsymbol{z})-\boldsymbol{\beta}\|^2_{\boldsymbol{Q}_{\hat{b}(\boldsymbol{z})}}. \tag{5}$$

The fixed solutions $\check{\boldsymbol{a}}$ and $\check{\boldsymbol{b}}$, i.e., the minimizers of (2), are now given by

$$\begin{aligned}\check{\boldsymbol{a}}&=\underset{\boldsymbol{z}\in\mathbb{Z}^n}{\operatorname{argmin}}\underbrace{\left(\|\hat{\boldsymbol{a}}-\boldsymbol{z}\|^2_{\boldsymbol{Q}_{\hat{a}}}+\left\|\hat{\boldsymbol{b}}(\boldsymbol{z})-\check{\boldsymbol{b}}(\boldsymbol{z})\right\|^2_{\boldsymbol{Q}_{\hat{b}(\boldsymbol{z})}}\right)}_{F(\boldsymbol{z})}\\ \check{\boldsymbol{b}}&=\check{\boldsymbol{b}}(\check{\boldsymbol{a}})\end{aligned} \tag{6}$$

If no constraint is imposed when estimating $\boldsymbol{b}$, so that $\mathcal{B}=\mathbb{R}^p$, then $\check{\boldsymbol{b}}(\boldsymbol{z})=\hat{\boldsymbol{b}}(\boldsymbol{z})$, resulting in the standard ILS solution $\check{\boldsymbol{a}}=\operatorname{argmin}_{\boldsymbol{z}\in\mathbb{Z}^n}\|\hat{\boldsymbol{a}}-\boldsymbol{z}\|^2_{\boldsymbol{Q}_{\hat{a}}}$ and $\check{\boldsymbol{b}}=\hat{\boldsymbol{b}}(\check{\boldsymbol{a}})$, which can be efficiently solved using for instance the LAMBDA method (Teunissen 1995).

Prominent examples for imposing constraints on $\boldsymbol{b}$ were formulated by using a-priori information on the local geometry of a multi-receiver setup on a rigid platform. In the *GNSS compass model* (Park and Teunissen 2009; Teunissen 2010), the baseline length in a single-baseline model is constrained as $\|\boldsymbol{b}\|=l$ and in the *multivariate GNSS attitude model* (Teunissen 2007; Giorgi et al. 2012), $\boldsymbol{b}$ is constrained to represent an orthonormal matrix characterizing the rotation of the moving platform wrt. the reference frame. The solutions of the respective problems are mechanized in the *constrained* C-LAMBDA and *multivariate-constrained* MC-LAMBDA methods.

Solving (6) generally includes a search for integer vectors $\boldsymbol{z}$ and an evaluation of the objective function $F(\boldsymbol{z})$ for each integer vector, which in turn implies solving the minimization problem (5). The search radius can be set by evaluating $F(\boldsymbol{z})$ for the unconstrained ILS ambiguity solution, potentially combined with a shrinking approach once a better solution has been found. Depending on the constraint, solving (5) might not be trivial and can be computationally demanding, in particular if many integer vectors are to be evaluated.

For the troposphere-bounded GNSS model, the feasible region $\mathcal{B}$ will be defined by means of *linear inequality constraints* rather than by *non-linear equality constraints* like in the above two examples. The corresponding solution of (5) will be shown in the following section.

The fixed solution $\check{\boldsymbol{b}}$ is normally rejected if the ambiguity SR is not sufficiently high, in order to limit the occurrence of large errors. In this case, the constraint $\boldsymbol{b}\in\mathcal{B}$ can still be utilized in a *constrained float solution*, in which the integer constraint on the estimate of $\boldsymbol{a}$ is disregarded. It can be derived by interchanging the roles of $\hat{\boldsymbol{a}}$ and $\hat{\boldsymbol{b}}(\boldsymbol{z})$ in (4) to $\hat{\boldsymbol{b}}$ and $\hat{\boldsymbol{a}}(\boldsymbol{\beta})$ (Giorgi 2011) and follows as

$$\hat{\boldsymbol{b}}_{\mathrm{c}}=\underset{\boldsymbol{\beta}\in\mathcal{B}}{\operatorname{argmin}}\|\hat{\boldsymbol{b}}-\boldsymbol{\beta}\|^2_{\boldsymbol{Q}_{\hat{b}}} \tag{7}$$

$$\hat{\boldsymbol{a}}_{\mathrm{c}}=\hat{\boldsymbol{a}}\left(\hat{\boldsymbol{b}}_{\mathrm{c}}\right), \tag{8}$$

where usually one is only interested in $\hat{\boldsymbol{b}}_{\mathrm{c}}$, which requires solving the same problem as in (5) with a different weighting matrix.

The troposphere-bounded GNSS solution

The wet component of the tropospheric delay accounts for ~10% of the total tropospheric delay, so that the true ZWD roughly assumes values of $0-30\mathrm{cm}$, depending on the meteorologic conditions and the receiver location. When estimating a ZWD parameter in GNSS positioning applications, a high correlation is obtained between the estimates of the ZWD and the up component of the user position. For short observation time spans, the estimation precision of the ZWD can reach several meters, which means that most likely the resulting estimate is physically unrealistic. He (2025) presented the idea to limit the estimated ZWD to its

physically possible values, so that unrealistically small or large estimates are avoided. The limits can for instance be found by evaluating one of the ZWD models that depend on surface meteorologic conditions (Mendes 1999) for the minimum and maximum expectable and/or feasible temperature and relative humidity. A simpler way can also be to make use of conservative bounds obtained from past observations.

Let $\boldsymbol{e}_\tau$ be a p-dimensional unit vector with a "1" entry at the index of the ZWD parameter in $\boldsymbol{b}$. The feasible region $\mathcal{B}$ can now be formulated as

$$\mathcal{B} = \left\{ \boldsymbol{\beta} \in \mathbb{R}^p | \boldsymbol{e}_\tau^{\mathrm{T}} \boldsymbol{\beta} \geq \tau_{\min}, \boldsymbol{e}_\tau^{\mathrm{T}} \boldsymbol{\beta} \leq \tau_{\max} \right\}. \tag{9}$$

With this definition of the feasible region, (5) and (7) are *quadratic optimization problems with linear constraints* and therefore convex optimization problems (Boyd and Vandenberghe 2004). Such problems can for instance be numerically solved with subgradient based dual methods. In our case with only a single bounded variable, however, a simpler solution can be found. For the sake of simplicity, we base our derivations on the notation of (7), but the results can easily be transferred to (5) by replacing the float estimate $\hat{\boldsymbol{b}}$ by the conditional estimate $\hat{\boldsymbol{b}}(\boldsymbol{z})$ with its respective covariance matrix.

The solution of (7) with the feasible region (9) is derived in Appendix A as

$$\hat{\boldsymbol{b}}_{\mathrm{c}} = \begin{cases} \hat{\boldsymbol{b}} - \left(\boldsymbol{Q}_{\hat{\boldsymbol{b}}} \boldsymbol{e}_\tau\right) Q_{\hat{\tau}}^{-1} \left(\hat{\tau} - \tau_{\min}\right), & \hat{\tau} < \tau_{\min} \\ \hat{\boldsymbol{b}}, & \tau_{\min} \leq \hat{\tau} \leq \tau_{\max} \\ \hat{\boldsymbol{b}} - \left(\boldsymbol{Q}_{\hat{\boldsymbol{b}}} \boldsymbol{e}_\tau\right) Q_{\hat{\tau}}^{-1} \left(\hat{\tau} - \tau_{\max}\right), & \hat{\tau} > \tau_{\max} \end{cases} \tag{10}$$

with $\hat{\tau} = \boldsymbol{e}_\tau^{\mathrm{T}} \hat{\boldsymbol{b}}$ and $Q_{\hat{\tau}} = \boldsymbol{e}_\tau^{\mathrm{T}} \boldsymbol{Q}_{\hat{\boldsymbol{b}}} \boldsymbol{e}_\tau$. This result can be understood as follows: If the unconstrained float solution falls within the feasible region $\hat{\boldsymbol{b}} \in \mathcal{B}$, it is simply left unchanged. If the estimated ZWD $\hat{\tau} < \tau_{\min}$ is too small, then it is increased to $\tau_{\min}$, and if the estimated ZWD $\hat{\tau} > \tau_{\max}$ is too large, it is decreased to $\tau_{\max}$ in $\hat{\boldsymbol{b}}_{\mathrm{c}}$. The other entries of $\hat{\boldsymbol{b}}_{\mathrm{c}}$ are the conditional estimates assuming the ZWD parameter is given as $\tau_{\min}$ or $\tau_{\max}$, respectively.

An equivalent formulation of the feasible region $\mathcal{B}$ in (9) is given by

$$\mathcal{B} = \left\{ \boldsymbol{\beta} \in \mathbb{R}^p | \left\| \boldsymbol{e}_\tau^{\mathrm{T}} \boldsymbol{\beta} - \tau_{\mathrm{mean}} \right\| \leq \tau_{\mathrm{rad}} \right\} \tag{11}$$

with $\tau_{\mathrm{mean}} = (\tau_{\max} + \tau_{\min})/2$ and $\tau_{\mathrm{rad}} = (\tau_{\max} - \tau_{\min})/2$, i.e., the two linear inequality constraints can be written as a single quadratic inequality constraint, similar to the length constraint of the GNSS compass problem. The constraint will only be active and then act as an equality constraint if $\hat{\boldsymbol{b}} \notin \mathcal{B}$, so that the troposphere-bounded model is mathematically a special case of the constrained ILS models presented in the literature, cf. the previous section.

If the bounds in (10) are chosen very tight, so that $(\tau_{\max} - \tau_{\min}) \to 0$ and both bounds become identical, the troposphere-bounded model becomes identical to the troposphere-fixed model in which the ZWD is fixed to one of the identical bounds. If both bounds are chosen very far from τ as $(\tau - \tau_{\min}) \to \infty$ and $(\tau_{\max} - \tau) \to \infty$, the bounds will never be active and the troposphere-bounded model is identical to the troposphere-float model, in which no constraints are imposed on the ZWD.

With the minimizer of (7) given in (10), the minimum can easily be derived as

$$\left\| \hat{\boldsymbol{b}} - \hat{\boldsymbol{b}}_{\mathrm{c}} \right\|_{\boldsymbol{Q}_{\hat{\boldsymbol{b}}}}^2 = \begin{cases} Q_{\hat{\tau}}^{-1} (\hat{\tau} - \tau_{\min})^2, & \hat{\tau} < \tau_{\min} \\ 0, & \tau_{\min} \leq \hat{\tau} \leq \tau_{\max} \\ Q_{\hat{\tau}}^{-1} (\hat{\tau} - \tau_{\max})^2, & \hat{\tau} > \tau_{\max} \end{cases} \tag{12}$$

and only depends on the constrained ZWD estimate. This is relevant for the constrained ILS problem (6), in which the objective function $F(\boldsymbol{z})$ has to be evaluated for potentially many integer vectors $\boldsymbol{z}$. The first term of $F(\boldsymbol{z})$, $\|\hat{\boldsymbol{a}} - \boldsymbol{z}\|_{\boldsymbol{Q}_{\hat{\boldsymbol{a}}}}^2$, is already available from the integer search. The second term, $\|\hat{\boldsymbol{b}}(\boldsymbol{z}) - \check{\boldsymbol{b}}(\boldsymbol{z})\|_{\boldsymbol{Q}_{\hat{\boldsymbol{b}}(\boldsymbol{z})}}^2$, is of the same type as (12), so that if $\hat{\tau}(\boldsymbol{z}) = \boldsymbol{e}_\tau^{\mathrm{T}} \hat{\boldsymbol{b}}(\boldsymbol{z})$ falls within the interval $[\tau_{\min}, \tau_{\max}]$, it is zero, whereas for $\hat{\tau}(\boldsymbol{z}) < \tau_{\min}$, it is $Q_{\hat{\tau}(\boldsymbol{z})}^{-1} (\hat{\tau}(\boldsymbol{z}) - \tau_{\min})^2$ with $Q_{\hat{\tau}(\boldsymbol{z})} = \boldsymbol{e}_\tau^{\mathrm{T}} \boldsymbol{Q}_{\hat{\boldsymbol{b}}(\boldsymbol{z})} \boldsymbol{e}_\tau$, and for $\hat{\tau}(\boldsymbol{z}) > \tau_{\max}$ analogously.

In order to discuss the distributional properties of the troposphere-bounded solution (10), let the float estimate be composed as $\hat{\boldsymbol{b}} = \left[\hat{\tilde{\boldsymbol{b}}}^{\mathrm{T}}, \hat{\tau}\right]^{\mathrm{T}}$, and $\hat{\boldsymbol{b}}_{\mathrm{c}}$ analogously. As explained in Appendix A, $\hat{\boldsymbol{b}}_{\mathrm{c}}$ can be computed by first computing the estimate $\hat{\tau}_{\mathrm{c}} \in [\tau_{\min}, \tau_{\max}]$ based on $\hat{\tau}$, and then by computing the conditional estimate $\hat{\tilde{\boldsymbol{b}}}(\hat{\tau}_{\mathrm{c}})$. The constrained ZWD estimate $\hat{\tau}_{\mathrm{c}}$ is characterized by a hybrid probability density function (pdf)/probability mass function $f_{\hat{\tau}_{\mathrm{c}}}(\cdot)$. Its non-zero values are given by

$$f_{\hat{\tau}_{\mathrm{c}}}(t) = \begin{cases} P(\hat{\tau} < \tau_{\min}), & t = \tau_{\min} \\ f_{\hat{\tau}}(t), & \tau_{\min} \leq t \leq \tau_{\max} \\ P(\hat{\tau} > \tau_{\max}), & t = \tau_{\max} \end{cases} \tag{13}$$

with $f_{\hat{\tau}}(\cdot)$ the pdf of $\hat{\tau}$ and $P(\cdot)$ the probability of an event. That is, $\hat{\tau}_{\mathrm{c}}$ assumes the two boundary values with a certain probability, and between these two values it follows the Gaussian distribution of the unconstrained float solution $\hat{\tau}$. Since $\hat{\tau}_{\mathrm{c}}$ is derived only from $\hat{\tau}$, the pdf of $\hat{\tilde{\boldsymbol{b}}}_{\mathrm{c}}$ can be formulated using the conditional pdf $f_{\hat{\tilde{\boldsymbol{b}}}|\hat{\tau}}(\cdot|\cdot)$ as

$$f_{\hat{\check{\boldsymbol{b}}}_{\mathrm{c}}}\left(\tilde{\boldsymbol{\beta}}\right) = f_{\hat{\check{\boldsymbol{b}}}|\hat{\tau}}\left(\tilde{\boldsymbol{\beta}}|\tau_{\min}\right) P\left(\hat{\tau} < \tau_{\min}\right) + \int_{\tau_{\min}}^{\tau_{\max}} f_{\hat{\check{\boldsymbol{b}}}|\hat{\tau}}\left(\tilde{\boldsymbol{\beta}}|t\right) f_{\hat{\tau}}\left(t\right) \mathrm{d}t + f_{\hat{\check{\boldsymbol{b}}}|\hat{\tau}}\left(\tilde{\boldsymbol{\beta}}|\tau_{\max}\right) P\left(\hat{\tau} > \tau_{\max}\right). \tag{14}$$

It is the sum of two weighted conditional Gaussian distributions for the two troposphere bounds with the probabilities from (13), and a non-Gaussian contribution from integrating the joint pdf of $\hat{\check{\boldsymbol{b}}}$ and $\hat{\tau}$ over the troposphere interval $[\tau_{\min}, \tau_{\max}]$.

The expectation of $\hat{\tau}_{\mathrm{c}}$ follows from (13) as

$$\mathrm{E}\left[\hat{\tau}_{\mathrm{c}}\right] = P\left(\hat{\tau} < \tau_{\min}\right) \cdot \tau_{\min} + \int_{\tau_{\min}}^{\tau_{\max}} f_{\hat{\tau}}\left(t\right) \cdot t \, \mathrm{d}t + P\left(\hat{\tau} > \tau_{\max}\right) \cdot \tau_{\max}. \tag{15}$$

If the bounds $\tau_{\min}$ and $\tau_{\max}$ are symmetric around τ, the two probabilities in (15) are identical and $\tau_{\min} + \tau_{\max} = 2\tau$, so that the first and third term of (15) add to $2P\left(\hat{\tau} < \tau_{\min}\right) \cdot \tau$. As $f_{\hat{\tau}}\left(t\right)$ is symmetric around τ, the second term of (15) follows as $\left[1 - 2P\left(\hat{\tau} < \tau_{\min}\right)\right] \cdot \tau$, so that $\mathrm{E}\left[\hat{\tau}_{\mathrm{c}}\right] = \tau$. Under the given model assumptions, the conditional estimate $\hat{\check{\boldsymbol{b}}}_{\mathrm{c}} = \hat{\check{\boldsymbol{b}}}(\hat{\tau}_{\mathrm{c}})$ is unbiased if $\hat{\tau}_{\mathrm{c}}$ is unbiased, so that $\mathrm{E}\left[\hat{\check{\boldsymbol{b}}}_{\mathrm{c}}\right] = \boldsymbol{b}$ if the bounds are symmetric around τ.

Two examples of the distributions (13) and (14) are shown in Fig. 1. They follow from a PPP example, where the top panels show the distribution of the estimates of the ZWD parameter τ and the bottom panels the distribution of the up-component of the user position. The left panels correspond to $\tau_{\min} = \tau - 10\mathrm{cm}$ and $\tau_{\max} = \tau + 10\mathrm{cm}$, i.e., the troposphere bounds are symmetric around the true value, whereas the right panels correspond to $\tau_{\min} = \tau - 17.5\mathrm{cm}$ and $\tau_{\max} = \tau + 2.5\mathrm{cm}$. In the top panels we can see the Gaussian error distribution of the unconstrained float solution $\hat{\tau}$ in gray. The error distribution of the constrained solution $\hat{\tau}_{\mathrm{c}}$ in blue is composed of the two discrete probability masses at $\tau_{\min}$ and $\tau_{\max}$, and in between the part of the Gaussian distribution of $\hat{\tau}$. In the bottom panels we can see that the corresponding distributions of the troposphere-constrained up solutions in blue, taken from $\hat{\check{\boldsymbol{b}}}_{\mathrm{c}}$, are more peaked than the unconstrained float solution in gray. The three components of the blue curves, cf. (14), are shown as dashed lines, where the red and yellow components are the weighted conditional Gaussian distributions from the troposphere bounds together with their conditional means in black, as indicated by the red and yellow markers in the top panels, and the blue component is the second term in (14) from the continuous part of $\hat{\tau}_{\mathrm{c}}$. We can see that if the tropospheric bounds are symmetric around the true but unknown τ, the two weighted conditional Gaussians are biased but symmetric around the true value, and the dashed blue curve is an unbiased distribution, so that the constrained solution $\hat{\boldsymbol{b}}_{\mathrm{c}}$ is unbiased. In the right panels this is clearly not the case, as the red and yellow curve have different weights and biases of different magnitude, and the blue dashed curve is also not an unbiased distribution, so that $\hat{\boldsymbol{b}}_{\mathrm{c}}$ is biased, as can be seen from the solid blue curve.

So far we only discussed the distributional properties of the conditional float solution $\hat{\boldsymbol{b}}_{\mathrm{c}}$ in (7), not of the fixed solution $\check{\boldsymbol{b}}$ in (6). Deriving a useful expression for the pdf of $\check{\boldsymbol{b}}$ is more difficult, as in addition to the parameter bounds also the discrete random nature of the fixed ambiguity solution $\check{\boldsymbol{a}}$ has to be accounted for. In the case that the probability of

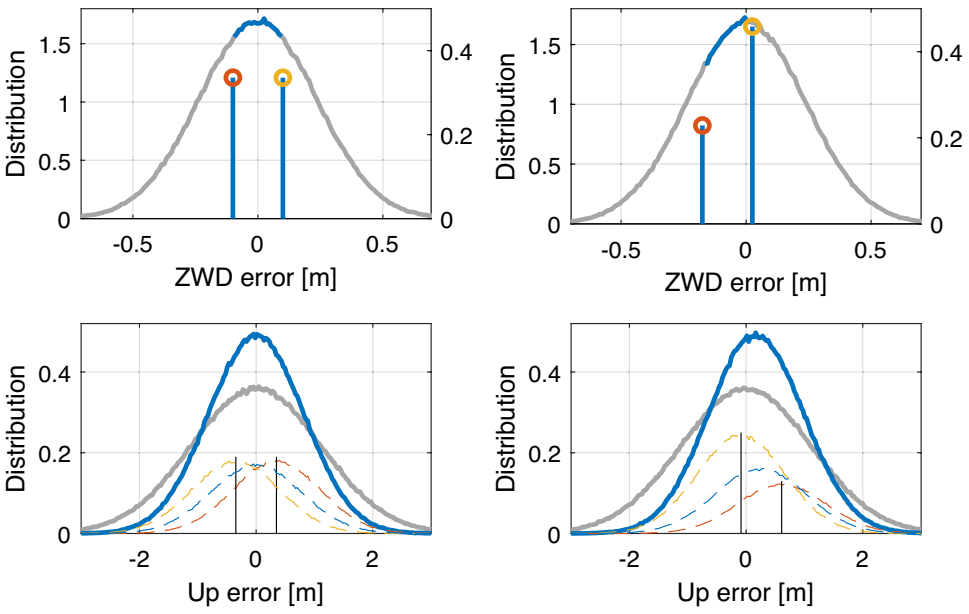

Fig. 1 Distribution functions of the ZWD parameter (top) and the up-component of the user position (bottom) for a PPP example, where the unconstrained float solution $\hat{\boldsymbol{b}}$ is shown in gray and the constrained float solution $\hat{\boldsymbol{b}}_{\mathrm{c}}$ in blue. In the left panels, the ZWD bounds $\tau_{\min}$ and $\tau_{\max}$ are symmetric around the true value τ, leading to unbiased estimates. In the right panels, τ is significantly closer to the upper bound $\tau_{\max}$, leading to a bias of the ZWD estimate of −5.1 cm and of the up-component of 17.8 cm

correct ambiguity resolution $P(\check{\boldsymbol{a}} = \boldsymbol{a})$ is sufficiently high, one can work with the assumption that $\check{\boldsymbol{a}}$ is deterministic. The properties of the fixed estimate $\check{\boldsymbol{b}}$ can then be discussed in the same way as the ones of the conditional float solution $\hat{\boldsymbol{b}}_{\mathrm{c}}$, but with the conditional covariance matrix $\boldsymbol{Q}_{\hat{\boldsymbol{b}}(z)}$ instead of $\boldsymbol{Q}_{\hat{\boldsymbol{b}}}$. We note, however, that the conditional precision of the ZWD estimate in the fixed solution might often be considerably smaller than the interval given by the bounds $\tau_{\min}$ and $\tau_{\max}$. This implies that when the ambiguities are resolved correctly, with a high probability the troposphere bounds are not active, so that the benefits of the ZWD constraint for the fixed solution are then mostly an increased ILS SR and/or a shorter time-to-first-fix (TTFF), rather than an improved precision from the troposphere bounds.

The above model only contains one bounded parameter, the ZWD, so that only a single constraint can be active at a time and a simple solution is found in (10). The concept of defining feasible intervals can be extended to multiple parameters, for instance to horizontal tropospheric gradients, leading to additional constraints when defining the feasible region $\mathcal{B}$ in (9). The solution of such a problem follows the principle of (10), namely for $\hat{\boldsymbol{b}} \in \mathcal{B}$ the solution is left unchanged, and otherwise it will lie on the boundary of $\mathcal{B}$. In the latter case it is, however, not obvious from $\hat{\boldsymbol{b}}$ which of the constraints are active at the optimum, as now more than one constraint can be active. Once the set of active constraints is found, the corresponding equality-constrained solution is easily derived by fixing the values of the respective parameters. An alternative to the above mentioned numerical subgradient based dual methods are therefore *active set methods* (Nocedal and Wright 2006), especially with only a few bounded parameters, in which different candidate sets of active constraints are evaluated iteratively until a valid solution meeting the Karush–Kuhn–Tucker (KKT) conditions is found.

Experimental validation

While (1) covers a wide range of GNSS applications, we focus on kinematic multi-GNSS multi-frequency PPP/PPP-RTK user models. In particular, $\boldsymbol{y}$ contains undifferenced, uncombined phase and code observations of the rover receiver, to which external corrections for the satellite clock offsets, phase biases, and code biases are applied. The estimated parameters $\boldsymbol{b}$ contain the receiver coordinates, the receiver clock offsets and frequency specific receiver phase and code biases, the ionospheric slant delays, and the tropospheric ZWD. The ambiguity vector $\boldsymbol{a}$ contains the double-difference integer ambiguities.

The following analyses are based on one day of simulated and real GPS and Galileo data from the user station PERT (Trimble Alloy) during March 15, 2025, using signals from up to five frequencies with a sampling rate of 30s and an elevation cut-off angle of 10°. The employed signals and their zenith-referenced standards are given in Table 1. Dual-frequency refers to GPS L1+L2 and Galileo E1+E5a, for triple-frequency the L5 and E6 signals are added, and for the five-frequency case also the Galileo E5b and E5 signals. The PPP corrections are computed on an epoch-by-epoch basis from the station NNOR (Septentrio PolaRx5TR) and applied by the user with zero latency and full covariance information. Precise orbits are taken from the GFZ rapid product (Männel et al. 2020). The GMF is used to estimate the ZWD parameters. For the real-data analyses, zenith hydrostatic delays are computed from the Saastamoinen model. We assume that biases, ambiguities, and the ZWD are time-constant, where the latter is valid as we only consider short time spans, whereas coordinates, ionospheric delays, and clock offsets are assumed completely unlinked in time. For more details on the observation model, see Brack et al. (2023).

We expect two main advantages from including bounds on the ZWD parameter in the positioning model, an illustration of which are shown in Fig. 2. It shows the convergence of the estimated ZWD and coordinate up component of a simulated dual-frequency GPS example, where the results of the troposphere-float model are shown in gray and of the troposphere-bounded model in blue. Left of the vertical lines, the solutions are float solutions for which we expect a precision improvement from bounding the ZWD estimate. We can see that in the unconstrained case in gray the large negative ZWD errors in the first epochs lead to large positive errors of the up component. For the troposphere-bounded model, we assume the bounds $\tau_{\min}$ and $\tau_{\max}$ are at $\mp 10\mathrm{cm}$ from the true ZWD as indicated by the dashed red lines. Bounding the float ZWD error in the constrained float solution in blue, cf. (7), clearly reduces the resulting up error. The second expected advantage is for the TTFF the ambiguities, where our criterion is an ILS SR of 99.9% or higher. In this example, the TTFF is clearly reduced from 15.0min with the troposphere-float model to 11.5min with the troposphere-bounded model, as indicated by the two vertical lines of the respective colors. The ambiguity-fixed solutions

Table 1 Employed signals with the estimated zenith-referenced standard deviations (std) of the code observations

	GPS			Galileo				
Freq	L1	L2	L5	E1	E5a	E5b	E5	E6
Std [cm]	28	22	25	21	21	21	12	23

For all carrier-phases a value of 2mm is assumed

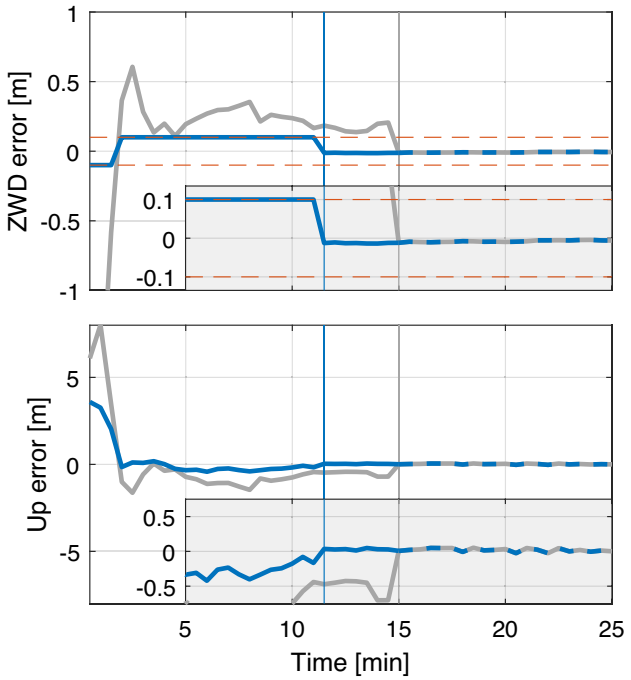

Fig. 2 Estimation error of ZWD and up component for a simulated dual-frequency GPS positioning example, where gray corresponds to the troposphere-float model and blue to the troposphere-bounded model. The vertical lines mark the times of ambiguity fixing, after which the float solutions switch to fixed solutions

right of the vertical lines show an immediate reduction of the errors, but are of similar precision for both models, as we can see in the two zoom-in plots at the bottom. These two advantages are evaluated in more detail in the following two sections via simulations and with real GNSS data.

Simulation results

Simulated positioning errors of a specific dual-frequency GPS+Galileo observation geometry using four observation epochs are shown in Fig. 3 for the troposphere-float, troposphere-bounded, and troposphere-fixed models. For the troposphere-bounded model, the bounds are chosen as $\tau \mp 10\text{cm}$. The respective float solutions are again shown in gray for the three coordinates and the ZWD, where of course for the troposphere-fixed model no ZWD parameter is present. The RMS positioning errors for the three models are listed on the bottom right and show that constraining or eliminating the ZWD parameter mostly improves the up component, so we will only focus on this one in the following. The ILS solutions are shown in green and red for correct and incorrect ambiguity estimates. We clearly see a decrease of the number of red points from the troposphere-float model, that uses no a-priori information on the ZWD, to the troposphere-fixed model with perfect a-priori information. As expected, the performance of the troposphere-bounded model lies in between. This optical impression is confirmed by the given ILS SRs of 35.5%, 47.2%, and 63.3%.

In Fig. 4, the impact of the ZWD bounds on the ambiguity-float positioning error is investigated for the dual-frequency GPS and GPS+Galileo cases. The convergence of the RMS errors of the ZWD and the up component are shown for the troposphere-float model in gray, the troposphere-fixed model in red, and the troposphere-bounded model in blue, where dark to light shades correspond to different bounds of $\tau \mp 2.5\text{cm}$, 5cm, 10cm, 15cm, and 20cm. The results

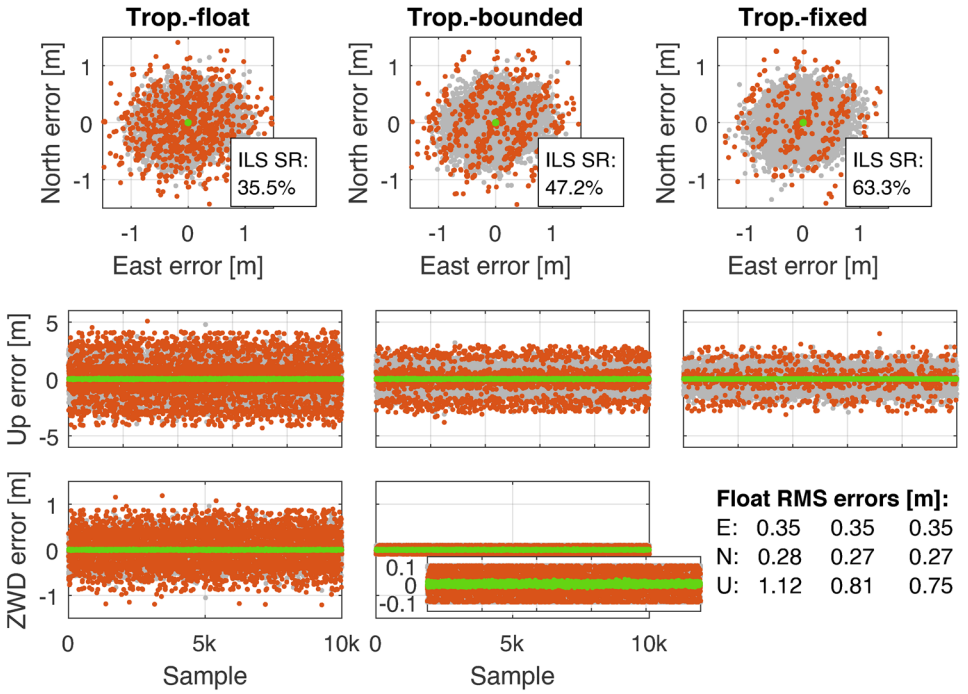

Fig. 3 Simulated east, north, up, and ZWD errors from a dual-frequency GPS+Galileo positioning example with four observation epochs for three troposphere models. The float solutions are shown in gray and the ILS solutions in green and red for correct and incorrect ambiguity estimates

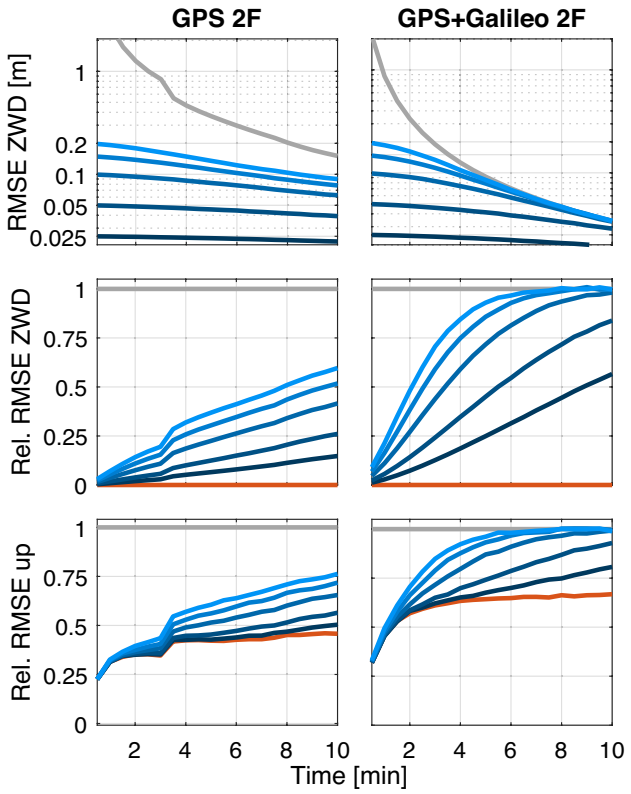

Fig. 4 Average simulated ambiguity-float RMS estimation errors of the ZWD and the up-component for the troposphere-float model (gray), the troposphere-fixed model (red), and the troposphere-bounded model (blue), for which darker shades imply tighter constraints. The RMS values in the two bottom rows are relative to the troposphere-float model

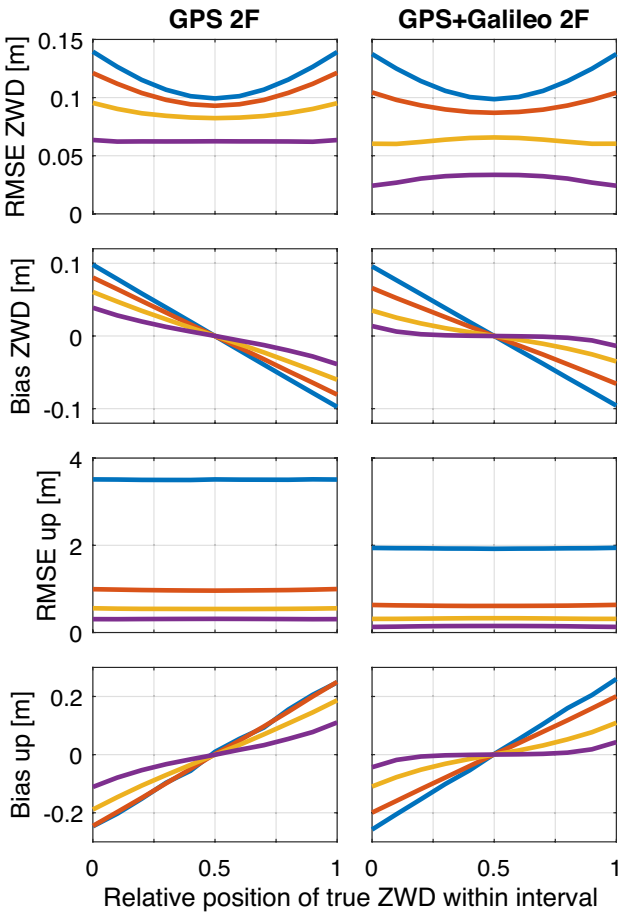

Fig. 5 Average simulated ambiguity-float RMS estimation errors and biases of the ZWD and the up-component for the troposphere-bounded model depending on the position of the true ZWD within a constraint interval of 20 cm length for observation times of 0.5 (blue), 2.5 (red), 5 (yellow) and 10 min (purple)

are averaged over 24 experiments starting at each full hour. The top row shows that the absolute ZWD RMS estimation errors of the troposphere-bounded model are essentially identical to the one-sided bounds in the first epochs, meaning that the bounds are active with a very high probability due to the low precision of the unconstrained float solution. Over time, when the precision of the ZWD estimates with the troposphere-float model increases, the bounds are less likely to be active and the troposphere-bounded model slowly converges to the troposphere-float model. The middle and bottom rows show the ZWD and up RMS estimation errors relative to the ones of the troposphere-float model. Even relatively loose bounds of $\tau \mp 20\mathrm{cm}$ lead to a ZWD RMS error reduction of more than 90% in the first epoch, which translates to a reduction of the up RMS error in the bottom row of ∼75% for GPS and ∼65% for GPS+Galileo, similar to what can be achieved with the troposphere-fixed model in red. With the convergence of the troposphere-float model, the relative improvement decreases, depending on how tight the ZWD bounds are. The cases with three and five frequencies lead to similar results and are not shown in detail.

Figure 5 shows the corresponding results if τ is no longer in the center of the constraint interval. We consider an interval of length $\tau_{\max} - \tau_{\min} = 20\mathrm{cm}$, where the horizontal axis reaches from $\tau = \tau_{\min}$ on the left to $\tau = \tau_{\max}$ on the right. As discussed in Fig. 1, the ZWD estimates are biased if the feasible interval is not centered around τ, where larger biases are observed towards the boundaries of the interval, see second row. With more epochs, the probability of the constraints being active gets smaller and the average bias is reduced. The ZWD RMS errors in the top row clearly also depend on the relative position of τ within the feasible interval, where larger values are observed towards the boundaries if $\hat{\tau}$ is of low precision compared to the length of the constraint interval, see for instance the blue curves corresponding to a single observation epoch, and smaller values if $\hat{\tau}$ is of high precision compared to the length of the interval, see the purple curve for combined GPS+Galileo. The ZWD biases propagate to the up-component, see bottom row, so that the bounds $\tau_{\min}$ and $\tau_{\max}$ should be preferably

symmetric around the unknown τ, and a user should be aware of potentially biased solutions. The up RMS errors in the third row are barely affected by the relative position of τ. We note that the biases are around one order of magnitude smaller than RMS errors of the constrained and unconstrained float solutions.

We will now discuss the ambiguity-fixed solutions using unconstrained and constrained ILS. Earlier it was claimed that the troposphere-bounded model is mostly expected to increase the ILS SR, not so much to improve the precision of a correctly fixed solution. To demonstrate this, the average ambiguity-fixed precision of the ZWD estimates resulting from the troposphere-float model is shown in Fig. 6 for two (purple), three (yellow), and five (green) frequencies, where *fixed precision* refers to the case that the ambiguities are assumed known. The thin lines represent the corresponding ILS SRs of the troposphere-fixed model, which is equivalent to the strongest case of the troposphere-bounded model in which the valid interval for the ZWD estimate only contains the value $\tau_{\min} = \tau_{\max}$. Whenever the SR is sufficiently high, so that a fixed solution can be accepted, the ambiguity-fixed ZWD precision is at the sub-centimeter level. The bounds would have to be at a similar level or tighter to have a noticeable impact on the estimates, see (5), which will usually not be the case.

This does not mean that the troposphere-bounded model is not beneficial for ambiguity-fixed solutions, as the constraints on the ZWD parameter can increase the ILS SR and lead to a shorter TTFF. Table 2 shows the average TTFFs in epochs for GPS and GPS+Galileo PPP-RTK with two, three, and five frequencies for the troposphere-float, the troposphere-fixed, and the troposphere-bounded model with different bounds. The fixing criterion is an ILS SR of at least 99.9%. The values in the parentheses show the reduction with respect to the troposphere-float model. Except for the dual-frequency GPS+Galileo case, assuming the ZWD parameter known (troposphere-fixed model) reduces the convergence time by roughly one third. With ZWD bounds of $\tau \mp 2.5\text{cm}$, the corresponding reduction is around 17.5%, and with $\tau \mp 10\text{cm}$, still a reduction of up to 10% is possible.

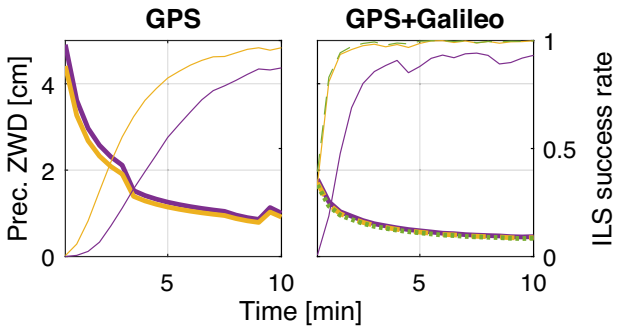

Fig. 6 Average ambiguity-fixed ZWD precision of the troposphere-float model (thick lines) and ILS SRs of the troposphere-fixed model (thin lines). Purple, yellow, and green lines correspond to the two, three and five frequency cases

Real-data results

The findings of the simulation results above are now validated with real GNSS data from the station PERT for the exemplary triple-frequency GPS+Galileo case. Positioning errors are computed with respect to precise a-priori coordinates. For the troposphere-bounded model, we set a lower bound of $\tau_{\min} = 0\text{cm}$ and an upper bound of $\tau_{\max} = 31\text{cm}$, which is derived from the ZWD model in Askne and Nordius (1987), using the maximum temperature during the day of $22.6°\text{C}$ and a relative humidity of 100%. The ZWD reference values from a daily dual-frequency GPS+Galileo PPP processing are shown in Fig. 7. They mostly lie within 15cm and 22cm, well below $\tau_{\max}$. The estimation is re-initialized every hour, and the following figures show the resulting 24 convergence periods.

The ambiguity-float east, north, and up positioning errors as well as the ZWD estimates are presented in Fig. 8 for the 24 convergence periods. The results of the troposphere-float and troposphere-bounded models are shown in gray and blue, respectively, together with their empirical RMS errors in black and red. While the horizontal components are only slightly different with almost identical RMS errors, we see a significant reduction of the up error with the troposphere-bounded model in the first epochs, where the blue lines are much more concentrated around zero. In the first epoch, the RMS error with the troposphere-float model is 5.4m, which

Table 2 Simulated average TTFF the ambiguities with the troposphere-float, the troposphere-fixed, and the troposphere-bounded models in epochs, where one epoch corresponds to 30s

Systems/freq	Trop. fixed	Trop. bounded					Trop. float
		$\tau \mp 2.5\text{cm}$	$\tau \mp 5\text{cm}$	$\tau \mp 10\text{cm}$	$\tau \mp 15\text{cm}$	$\tau \mp 20\text{cm}$	
GPS 2F	38.4 (30.7%)	46.7 (15.7%)	47.6 (14.1%)	52.8 (4.7%)	54.7 (1.3%)	54.8 (1.1%)	55.4
GPS 3F	28.5 (32.0%)	34.9 (16.7%)	37.9 (9.6%)	40.5 (3.3%)	41.0 (2.2%)	41.2 (1.7%)	41.9
GPS+Gal 2F	25.5 (6.9%)	26.7 (2.6%)	26.9 (1.8%)	26.9 (1.8%)	27.3 (0.4%)	27.0 (1.5%)	27.4
GPS+Gal 3F	7.4 (35.1%)	9.2 (19.3%)	9.8 (14.0%)	10.4 (8.8%)	10.5 (7.9%)	11.1 (2.6%)	11.4
GPS+Gal 5F	7.1 (35.5%)	9.0 (18.2%)	9.7 (11.8%)	9.9 (10.0%)	10.2 (7.3%)	10.8 (1.8%)	11.0

The values in parentheses are the reduction wrt. the troposphere-float model

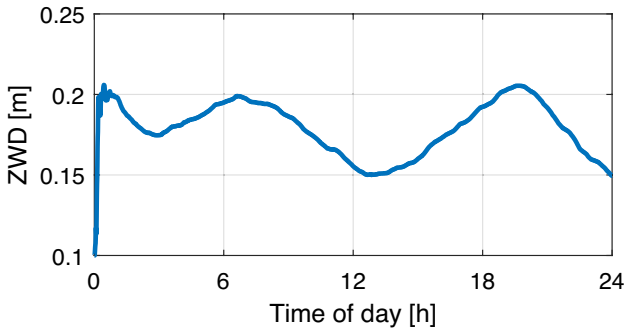

Fig. 7 Reference ZWD of station PERT during March 15, 2025, estimated from static dual-frequency GPS+Galileo PPP

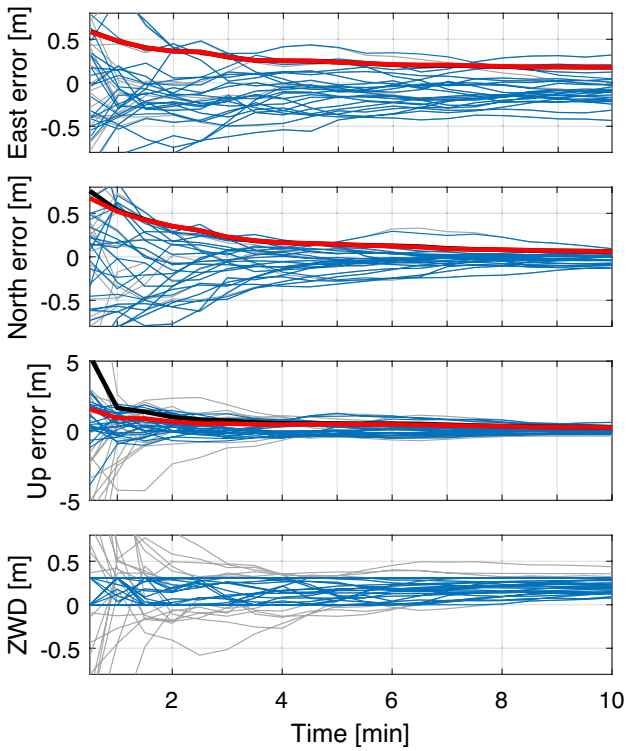

Fig. 8 Ambiguity-float positioning errors and ZWD estimates of triple-frequency GPS+Galileo PPP of the station PERT during March 15, 2025. Gray and blue lines correspond to 24 convergence periods with the troposphere-float and -bounded models, and the corresponding RMS errors are shown in black and red

is reduced by more than 70% to 1.6m with the troposphere-bounded model. The last panel shows the corresponding ZWD estimates, where the blue lines are confined to the interval between $\tau_{\min}$ and $\tau_{\max}$.

Ambiguity-fixed results are shown in Fig. 9 for the same 24 periods, where a solution is only available if the corresponding ILS SR is above 99.9%, so that the lines do not start in the first epoch. The TTFFs are marked with blue pluses and gray circles. The ILS SRs are computed via Monte Carlo integration using the computed variance and covariance matrices $\boldsymbol{Q}_{\hat{a}}$, $\boldsymbol{Q}_{\hat{b}}$, and $\boldsymbol{Q}_{\hat{b}\hat{a}}$, where for the

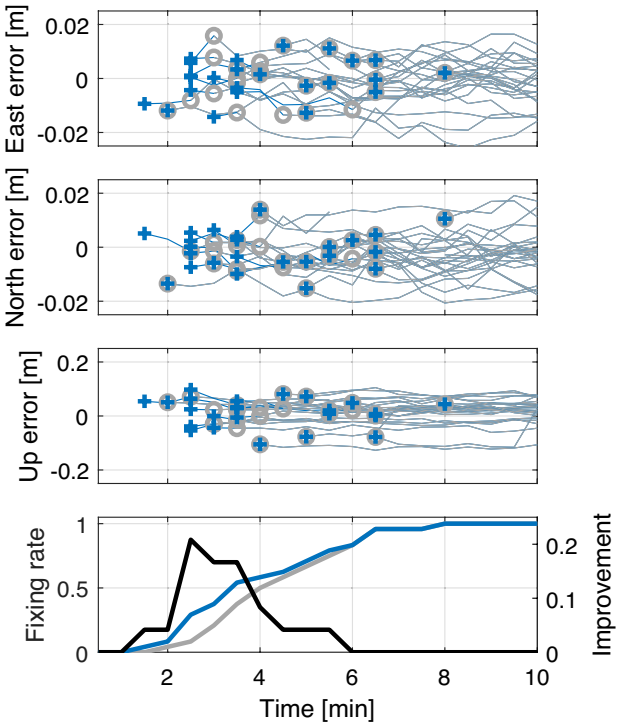

Fig. 9 Ambiguity-fixed positioning errors of triple-frequency GPS+Galileo PPP-RTK of the station PERT during March 15, 2025. Gray and blue lines correspond to 24 convergence periods with the troposphere-float and -bounded models, where only solutions with an ILS SR of at least 99.9% are included. The availability of fixed solutions is shown in the last panel, together with the improvement from the troposphere-bounded model in black

troposphere-bounded model it is assumed that the true but unknown ZWD τ is centered withing the interval $[\tau_{\min}, \tau_{\max}]$. We can see that generally the blue pluses appear earlier than the gray circles, demonstrating the increased SR of the constrained ILS. With the troposphere-float model, the average TTFF is 9.1 epochs, which is reduced by 9.2% to 8.2 epochs with the troposphere-bounded model, which is in agreement with Table 2. After both fixed solutions are available, however, they are essentially identical so that the gray lines cover the blue lines, meaning that in these examples the troposphere-bounds are not active and do not contribute to improve the precision of the fixed solution. The last row shows the average availability of both solutions, with an improvement of up to 21% with the troposphere-bounded model, as shown in black.

Setting the ZWD bounds

The basis of the troposphere-bounded model is the definition of valid ZWD bounds, and its performance is affected by the length $\tau_{\max} - \tau_{\min}$ of the constraint interval and the relative position of τ within this interval. By means of post-processed GNSS ZWD estimates for the year 2024 with a

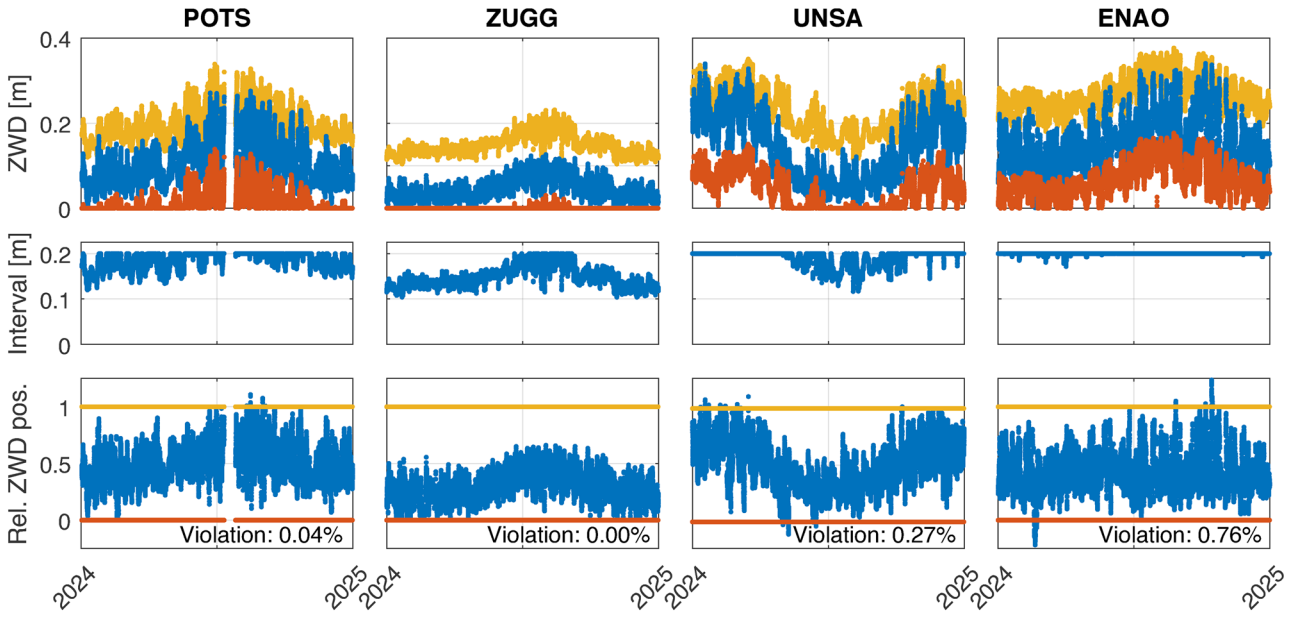

Fig. 10 Top: Estimated ZWD values of four selected sites computed with static GPS PPP during the year 2024 with 15 min resolution in blue, together with the lower and upper bounds in red and yellow. Middle: Length of constraint interval. Bottom: Relative position of true ZWD within the constraint interval and the percentage of points violating the interval

temporal resolution of 15min we verify whether a constraint interval of a few decimeter can reliably be determined for the case that ground meteorological data are available. We consider the four stations POTS (Potsdam, Germany), ZUGG (Zugspitze, Germany, at 2988m altitude), UNSA (Salta, Argentina), and ENAO (Santa Cruz da Graciosa, Graciosa Islands). The bounds $\tau_{\min}$ and $\tau_{\max}$ are simply set by evaluating the ZWD model of Askne and Nordius (1987) for the observed temperature and relative humidity, and by subtracting and adding 10cm, where $\tau_{\min}$ is also non-negative.

The ZWD estimates are shown in the first row of Fig. 10 in blue, together with the resulting bounds in red and yellow. We observe moderate ZWD values for POTS, low ZWD values for ZUGG due to the high altitude, strong seasonal fluctuations for UNSA, and generally larger values for ENAO. The length of the constraint interval that is limited to 20cm by this approach is shown in the middle row, where values smaller than 20cm indicate $\tau_{\min} = 0\text{cm}$, which is almost always the case for ZUGG and almost never for ENAO. The last row shows the relative position of the GNSS ZWD estimates within the constraint interval, where a value of 0.5 implies that the bounds are symmetric around the ZWD. While the values of POTS are relatively centered, the ones of ZUGG are generally closer to the lower bound, meaning that more restrictive upper bounds could be chosen to avoid biased solutions, cf. Figure 5. With 0.04% and 0.00%, the bounds for POTS and ZUGG are (almost) never violated, whereas for ENAO 0.76% of the ZWD values are outside the bounds, indicating that for this station the bounds should be chosen more conservatively. In general, one has to be very careful when setting the ZWD bounds, as an incorrect bound imposes a wrong constraint on the GNSS model that can adversely affect the positioning results, and only a lower bound of $\tau_{\min} = 0\text{cm}$ can always be guaranteed.

Conclusions

We introduced and discussed the troposphere-bounded GNSS model, in which the estimated ZWD is limited to a pre-defined interval. This was formulated by constraining the feasible set for the vector of real-valued parameters in the observation model. While the general framework for solving such constrained mixed integer models is known, the solution depends on the actual constraint. In this contribution, the solution for a single bounded parameter was derived, using either the KKT conditions or an orthogonal decomposition, see Appendix A. We presented both the constrained float solution in (7) and (10), and the constrained ILS solution in (6) and (10).

Distributional properties of the troposphere-bounded coordinate estimates were discussed, showing that bounding the ZWD can improve the precision of the constrained float solution, but also introduce a bias, if the bounds are not symmetric around the true value. Further, as the ZWD bounds will usually be chosen much looser than the precision of the ambiguity-fixed ZWD estimate, the troposphere-bounded model can mostly be expected to improve the SR and the TTFF by using the constrained ILS solution, not so

much the precision of the estimates, given that the ambiguity SR is sufficiently high.

These two benefits of the troposphere-bounded GNSS model were analyzed by means of simulated PPP examples with two, three, and five frequencies. The results showed that with the troposphere-bounded model we can expect a reduction of the average ambiguity-float up RMS error of ∼75% for GPS and ∼65% for GPS+Galileo in the first epoch, even with relatively loose ZWD bounds of $\mp 10\mathrm{cm}$ or more, see Fig. 4. Over time, when the solution converges, the bounds are less likely to be active and the benefit of the constrained solution slowly vanishes. For the ambiguity-fixed cases, the simulations showed that imposing a hard constraint on the ZWD parameter can be expected to reduce the TTFF on average by roughly one third compared to the troposphere-float model. With the troposphere-bounded model, ZWD bounds of $\mp 2.5\mathrm{cm}$ around the true value lead to a reduction of the TTFF of around 17.5%, and $\mp 10\mathrm{cm}$ still to a reduction of up to 10%, see Table 2. These findings were confirmed with real GNSS data recorded at the station PERT, see Figs. 8 and 9, where the ZWD estimates were constrained to lie within $0\mathrm{cm}$ and $31\mathrm{cm}$.

In practice, a main question is how to choose preferably tight but valid ZWD bounds $\tau_{\min}$ and $\tau_{\max}$, for instance utilizing ZWD models with measured and/or historical meteorological data and/or limits on their feasible values. A first analysis using the ZWD values of four stations during 2024 showed that reliable constraint intervals of a few decimeter can be determined in this way, where the local meteorological conditions should be taken into account.

Appendix A: Derivation of constrained solution

The constrained least-squares problem underlying (7) with the feasible region $\mathcal{B}$ defined in (9) can be written in standard form (Boyd and Vandenberghe 2004)

$$\min_{\boldsymbol{\beta}\in\mathbb{R}^p} f(\boldsymbol{\beta}) \text{ s.t.} g_1(\boldsymbol{\beta}) \le 0, g_2(\boldsymbol{\beta}) \le 0 \tag{A1}$$

with the objective function $f(\boldsymbol{\beta}) = \|\hat{\boldsymbol{b}} - \boldsymbol{\beta}\|^2_{\boldsymbol{Q}_{\hat{\boldsymbol{b}}}}$ and the constraints $g_1(\boldsymbol{\beta}) = \tau_{\min} - \boldsymbol{e}_\tau^{\mathrm{T}}\boldsymbol{\beta}$ and $g_2(\boldsymbol{\beta}) = \boldsymbol{e}_\tau^{\mathrm{T}}\boldsymbol{\beta} - \tau_{\max}$, with $\tau_{\min} < \tau_{\max}$. For this convex optimization problem, the Karush–Kuhn–Tucker (KKT) conditions are sufficient to find the global optimizer.

The *dual feasibility* condition evaluated at the optimizer $\hat{\boldsymbol{b}}_{\mathrm{c}}$ is given by $\nabla f\left(\hat{\boldsymbol{b}}_{\mathrm{c}}\right) + \lambda_1 \nabla g_1\left(\hat{\boldsymbol{b}}_{\mathrm{c}}\right) + \lambda_2 \nabla g_2\left(\hat{\boldsymbol{b}}_{\mathrm{c}}\right) = 0$, with the Lagrangian multipliers $\lambda_1, \lambda_2 \ge 0$, and follows from the above definitions as

$$\left(2\boldsymbol{Q}_{\hat{\boldsymbol{b}}}^{-1}\hat{\boldsymbol{b}}_{\mathrm{c}} - 2\boldsymbol{Q}_{\hat{\boldsymbol{b}}}^{-1}\hat{\boldsymbol{b}}\right) + (\lambda_2 - \lambda_1)\,\boldsymbol{e}_\tau = \boldsymbol{0}, \tag{A2}$$

so that the optimizer follows as

$$\hat{\boldsymbol{b}}_{\mathrm{c}} = \hat{\boldsymbol{b}} - \boldsymbol{Q}_{\hat{\boldsymbol{b}}}\boldsymbol{e}_\tau \frac{\lambda_2 - \lambda_1}{2}. \tag{A3}$$

We can now distinguish three cases from the *primal feasibility* condition:

1. $\boldsymbol{e}_\tau^{\mathrm{T}}\hat{\boldsymbol{b}} \ge \tau_{\min}$ and $\boldsymbol{e}_\tau^{\mathrm{T}}\hat{\boldsymbol{b}} \le \tau_{\max}$: The unconstrained solution $\hat{\boldsymbol{b}}$ already lies within the feasible region, so none of the two constraints is active ($\lambda_1 = \lambda_2 = 0$) and the constrained solution follows as $\hat{\boldsymbol{b}}_{\mathrm{c}} = \hat{\boldsymbol{b}}$.

2. $\boldsymbol{e}_\tau^{\mathrm{T}}\hat{\boldsymbol{b}} \le \tau_{\min}$: In order to increase $\boldsymbol{e}_\tau^{\mathrm{T}}\hat{\boldsymbol{b}}_{\mathrm{c}} = \boldsymbol{e}_\tau^{\mathrm{T}}\hat{\boldsymbol{b}} - \boldsymbol{e}_\tau^{\mathrm{T}}\boldsymbol{Q}_{\hat{\boldsymbol{b}}}\boldsymbol{e}_\tau \frac{\lambda_2-\lambda_1}{2}$, cf. (A3), as compared to $\boldsymbol{e}_\tau^{\mathrm{T}}\hat{\boldsymbol{b}}$, $\lambda_2 - \lambda_1$ has to be negative. As the Lagrangian multipliers are non-negative, and as only one of the constraints can be active (as $\tau_{\min} < \tau_{\max}$), this means that $\lambda_2 = 0$ and $\lambda_1 > 0$. The constraint $g_1\left(\hat{\boldsymbol{b}}_{\mathrm{c}}\right)$ being active means that $\boldsymbol{e}_\tau^{\mathrm{T}}\hat{\boldsymbol{b}}_{\mathrm{c}} = \tau_{\min}$, which finally leads to $\lambda_1 = 2\left(\boldsymbol{e}_\tau^{\mathrm{T}}\boldsymbol{Q}_{\hat{\boldsymbol{b}}}\boldsymbol{e}_\tau\right)^{-1}\left(\tau_{\min} - \boldsymbol{e}_\tau^{\mathrm{T}}\hat{\boldsymbol{b}}\right)$ and

$$\hat{\boldsymbol{b}}_{\mathrm{c}} = \hat{\boldsymbol{b}} - \left(\boldsymbol{Q}_{\hat{\boldsymbol{b}}}\boldsymbol{e}_\tau\right) Q_{\hat{\tau}}^{-1}(\hat{\tau} - \tau_{\min}), \tag{A4}$$

with $\hat{\tau} = \boldsymbol{e}_\tau^{\mathrm{T}}\hat{\boldsymbol{b}}$ and $Q_{\hat{\tau}} = \boldsymbol{e}_\tau^{\mathrm{T}}\boldsymbol{Q}_{\hat{\boldsymbol{b}}}\boldsymbol{e}_\tau$.

3. $\boldsymbol{e}_\tau^{\mathrm{T}}\hat{\boldsymbol{b}} \ge \tau_{\max}$: Following the derivation of the second case, now with the active constraint $g_2\left(\hat{\boldsymbol{b}}_{\mathrm{c}}\right)$, leads to

$$\hat{\boldsymbol{b}}_{\mathrm{c}} = \hat{\boldsymbol{b}} - \left(\boldsymbol{Q}_{\hat{\boldsymbol{b}}}\boldsymbol{e}_\tau\right) Q_{\hat{\tau}}^{-1}(\hat{\tau} - \tau_{\max}). \tag{A5}$$

As an alternative to using the KKT conditions, one could also use an orthogonal decomposition of $\hat{\boldsymbol{b}}$. Let $\hat{\boldsymbol{b}}$ be composed as $\hat{\boldsymbol{b}} = \left[\hat{\tilde{\boldsymbol{b}}}^{\mathrm{T}}, \hat{\tau}\right]^{\mathrm{T}}$, with $\hat{\tilde{\boldsymbol{b}}} \in \mathbb{R}^{p-1}$, and let $\hat{\tilde{\boldsymbol{b}}}(t)$ be the conditional estimate that assumes the value of the ZWD τ is given by t, with the conditional covariance matrix $\boldsymbol{Q}_{\hat{\tilde{\boldsymbol{b}}}(t)}$. With $\boldsymbol{\beta} = \left[\tilde{\boldsymbol{\beta}}^{\mathrm{T}}, t\right]^{\mathrm{T}}$, the objective function can now be decomposed as

$$\|\hat{\boldsymbol{b}} - \boldsymbol{\beta}\|^2_{\boldsymbol{Q}_{\hat{\boldsymbol{b}}}} = Q_{\hat{\tau}}^{-1}(\hat{\tau} - t)^2 + \|\hat{\tilde{\boldsymbol{b}}}(t) - \tilde{\boldsymbol{\beta}}\|^2_{\boldsymbol{Q}_{\hat{\tilde{\boldsymbol{b}}}(t)}}. \tag{A6}$$

We note that when applying the ZWD constraint, only the first term is affected. Minimizing (A6) over $\boldsymbol{\beta} \in \mathcal{B}$ means that we can now first minimize the first term over $t \in [\tau_{\min}, \tau_{\max}]$—which is easy as this is a scalar problem—and then choose $\tilde{\boldsymbol{\beta}}$ as the conditional estimate $\hat{\tilde{\boldsymbol{b}}}(t)$ to make the second term zero. It is easily verified that this solution is identical to the one derived above, since $\boldsymbol{Q}_{\hat{\boldsymbol{b}}}\boldsymbol{e}_\tau = \left[\boldsymbol{Q}_{\hat{\tilde{\boldsymbol{b}}}\hat{\tau}}^{\mathrm{T}}, Q_{\hat{\tau}}\right]^{\mathrm{T}}$.

Acknowledgements This work was initiated during the first author's stay at the Universidade Federal do Parana (UFPR) in Curitiba, Brazil, with Prof. Paulo Sergio de Oliveira Jr. as his host, for which funding was provided by Deutscher Akademischer Austauschdienst e.V. (DAAD).

Author contributions AB developed the theory, implemented the method, generated the results, and wrote the manuscript. SH developed the initial idea of including physical bounds for the tropospheric ZWD, supported the real-data analysis, contributed to the discussion about the content, and provided comments on the manuscript.

Funding Open Access funding enabled and organized by Projekt DEAL.

Data availability GNSS observation data used in this contribution are freely available through the International GNSS Service (IGS); for ZWD and meteorological data of 2024 see Dick et al. (2025).

Declarations

Competing interests The authors declare no competing interests.

References

Askne J, Nordius H (1987) Estimation of tropospheric delay for microwaves from surface weather data. Radio Sci 22(03):379–386. https://doi.org/10.1029/RS022i003p00379

Böhm J, Schuh H (2004) Vienna mapping functions in VLBI analyses. Geophys Res Lett. https://doi.org/10.1029/2003GL018984

Böhm J, Niell A, Tregoning P, Schuh H (2006) Global Mapping Function (GMF): a new empirical mapping function based on numerical weather model data. Geophys Res Lett. https://doi.org/10.1029/2005GL025546

Boyd SP, Vandenberghe L (2004) Convex optimization. Cambridge University Press

Brack A, Männel B, Schuh H (2023) On the feasibility of instantaneous multi-GNSS multi-frequency PPP-RTK. In: Proceedings of IEEE/ION PLANS 2023, Monterey, CA, USA. https://doi.org/10.1109/PLANS53410.2023.10140117

Dick G, Wickert J, Zus F, Männel B, Bradke M, Ramatschi M, Brandt A (2025) Gfz GNSS-derived tropospheric data products (global). GFZ Data Services. https://doi.org/10.5880/GFZ.IRZR.2025.003

Gao R, Ye F, Liu Y, Zha J, Odolinski R, Satirapod C, Zhang B (2024) Optimizing ZWD estimation strategies for enhanced PPP-RTK performance. GPS Solut 28(2):86. https://doi.org/10.1007/s10291-024-01629-3

Giorgi G (2011) GNSS carrier phase-based attitude determination - Estimation and applications. PhD Dissertation, Delft University of Technology, Delft, Netherlands

Giorgi G, Teunissen PJG, Verhagen S, Buist PJ (2012) Instantaneous ambiguity resolution in global-navigation-satellite-system-based attitude determination applications: a multivariate constrained approach. J Guid Control Dyn 35(1):51–67. https://doi.org/10.2514/1.54069

Hadas T, Teferle FN, Kazmierski K, Hordyniec P, Bosy J (2017) Optimum stochastic modeling for GNSS tropospheric delay estimation in real-time. GPS Solut 21:1069–1081. https://doi.org/10.1007/s10291-016-0595-0

He S (2025) On the asymmetric troposphere modeling in PPP. PhD Dissertation, University of Stuttgart, Stuttgart, Germany. https://doi.org/10.18419/opus-15649

Khodabandeh A (2022) Bias-bounded estimation of ambiguity: a method for radio interferometric positioning. IEEE Trans Signal Process 70:3042–3057. https://doi.org/10.1109/TSP.2022.3181344

Kleijer F (2004) Troposphere modeling and filtering for precise GPS leveling. PhD Dissertation, Delft University of Technology, Delft, Netherlands

Lagler K, Schindelegger M, Böhm J, Krásná H, Nilsson T (2013) GPT2: empirical slant delay model for radio space geodetic techniques. Geophys Res Lett 40(6):1069–1073. https://doi.org/10.1002/grl.50288

Männel B, Brandt A, Nischan T, Brack A, Sakic P, Bradke M (2020) Gfz rapid product series for the IGS. GFZ Data Services. https://doi.org/10.5880/GFZ.1.1.2020.003

Mendes VB (1999) Modeling the neutral-atmospheric propagation delay in radiometric space techniques. PhD Dissertation, Department of Geodesy and Geomatics Engineering Technical Report No. 199, University of New Brunswick, Fredericton, New Brunswick, Canada

Nocedal J, Wright SJ (2006) Numerical optimization. Springer, New York. https://doi.org/10.1007/978-0-387-40065-5

de Oliveira Jr PS, Morel L, Fund F, Legros R, Monico JFG, Durand S, Durand F (2017) Modeling tropospheric wet delays with dense and sparse network configurations for PPP-RTK. GPS Solut 21(1):237–250. https://doi.org/10.1007/s10291-016-0518-0

Park C, Teunissen PJG (2009) Integer least squares with quadratic equality constraints and its application to GNSS attitude determination systems. Int J Control Autom Syst 7(4):566–576. https://doi.org/10.1007/s12555-009-0408-0

Saastamoinen J (1972) Atmospheric correction for the troposphere and stratosphere in radio ranging satellites. Use Artif Satellites Geodesy 15:247–251. https://doi.org/10.1029/GM015p0247

Teunissen PJG (1993) Least-squares estimation of the integer GPS ambiguities. In: Invited lecture, section IV theory and methodology, IAG General Meeting, Beijing, China

Teunissen PJG (1995) The least-squares ambiguity decorrelation adjustment: a method for fast GPS integer ambiguity estimation. J Geod 70(1–2):65–82. https://doi.org/10.1007/BF00863419

Teunissen PJG (2007) A general multivariate formulation of the multi-antenna GNSS attitude determination problem. Artif Satell 42(2):97–111. https://doi.org/10.2478/v10018-008-0002-3

Teunissen PJG (2010) Integer least-squares theory for the GNSS compass. J Geod 84(7):433–447.

Teunissen PJG, Odijk D, Zhang B (2010) PPP-RTK: results of CORS network-based PPP with integer ambiguity resolution. J Aeronaut Astronaut Aviat Ser A 42(4):223–230. https://doi.org/10.6125/JoAAA.201012_42(4).02

Teunissen PJG, Giorgi G, Buist PJ (2011) Testing of a new single-frequency GNSS carrier phase attitude determination method: land, ship and aircraft experiments. GPS Solut 15:15–28. https://doi.org/10.1007/s10291-010-0164-x

Vaclavovic P, Dousa J, Elias M, Kostelecky J (2017) Using external tropospheric corrections to improve GNSS positioning of hot-air balloon. GPS Solut 21(4):1479–1489. https://doi.org/10.1007/s10291-017-0628-3

Wilgan K, Hadas T, Hordyniec P, Bosy J (2017) Real-time precise point positioning augmented with high-resolution numerical weather prediction model. GPS Solut 21:1341–1353. https://doi.org/10.1007/s10291-017-0617-6

Zumberge JF, Heflin MB, Jefferson DC, Watkins MM, Webb FH (1997) Precise point positioning for the efficient and robust analysis of GPS data from large networks. J Geophys Res 102(B3):5005–5017. https://doi.org/10.1029/96JB03860